The Astrophysical Journal, 950:95 (15pp), 2023 June 20 https://doi.org/10.3847/1538-4357/acd04c

Gemini Near Infrared Spectrograph–Distant Quasar Survey: Augmented Spectroscopic Catalog and a Prescription for Correcting UV-based Quasar Redshifts

Brandon M. Matthews[1], Cooper Dix[1], Ohad Shemmer[1], Michael S. Brotherton[2], Adam D. Myers[2], I. Andruchow[3,4], W. N. Brandt[5,6,7], S. C. Gallagher[8], Richard Green[9], Paulina Lira[10], Jacob N. McLane[2], Richard M. Plotkin[11,12], Gordon T. Richards[13], Jessie C. Runnoe[14], Donald P. Schneider[5,6], and Michael A. Strauss[15]
[1] Department of Physics, University of North Texas, Denton, TX 76203, USA; brandonmatthews@my.unt.edu
[2] Department of Physics and Astronomy, University of Wyoming, Laramie, WY 82071, USA
[3] Facultad de Ciencias Astronómicas y Geofísicas, Universidad Nacional de La Plata, Paseo del Bosque, B1900FWA La Plata, Argentina
[4] Instituto de Astrofísica de La Plata, CONICETUNLP, CCT La Plata, Paseo del Bosque, B1900FWA La Plata, Argentina
[5] Department of Astronomy and Astrophysics, The Pennsylvania State University, University Park, PA 16802, USA
[6] Institute for Gravitation and the Cosmos, The Pennsylvania State University, University Park, PA 16802, USA
[7] Department of Physics, 104 Davey Lab, The Pennsylvania State University, University Park, PA 16802, USA
[8] Department of Physics & Astronomy, University of Western Ontario, 1151 Richmond Street, London, ON N6C 1T7, Canada
[9] Steward Observatory, University of Arizona, 933 N Cherry Avenue, Tucson, AZ 85721, USA
[10] Departamento de Astronomía, Universidad de Chile, Casilla 36D, Santiago, Chile
[11] Department of Physics, University of Nevada, Reno, NV 89557, USA
[12] Nevada Center for Astrophysics, University of Nevada, Las Vegas, NV 89154, USA
[13] Department of Physics, Drexel University, 32 S. 32nd Street, Philadelphia, PA 19104, USA
[14] Department of Physics & Astronomy, Vanderbilt University, 6301 Stevenson Center Lane, Nashville, TN 37235, USA
[15] Department of Astrophysical Sciences, Princeton University, Princeton, NJ 08544, USA
Received 2022 December 1; revised 2023 April 18; accepted 2023 April 19; published 2023 June 13

Abstract

Quasars at $z \gtrsim 1$ most often have redshifts measured from rest-frame ultraviolet emission lines. One of the most common such lines, C IV λ1549, shows blueshifts up to $\approx$5000 km s^{-1} and in rare cases even higher. This blueshifting results in highly uncertain redshifts when compared to redshift determinations from rest-frame optical emission lines, e.g., from the narrow [O III] λ5007 feature. We present spectroscopic measurements for 260 sources at $1.55 \lesssim z \lesssim 3.50$ having $-28.0 \lesssim M_i \lesssim -30.0$ mag from the Gemini Near Infrared Spectrograph–Distant Quasar Survey (GNIRS-DQS) catalog, augmenting the previous iteration, which contained 226 of the 260 sources whose measurements are improved upon in this work. We obtain reliable systemic redshifts based on [O III] λ5007 for a subset of 121 sources, which we use to calibrate prescriptions for correcting UV-based redshifts. These prescriptions are based on a regression analysis involving C IV full-width-at-half-maximum intensity and equivalent width, along with the UV continuum luminosity at a rest-frame wavelength of 1350 Å. Applying these corrections can improve the accuracy and the precision in the C IV-based redshift by up to $\sim$850 km s^{-1} and $\sim$150 km s^{-1}, respectively, which correspond to $\sim$8.5 and $\sim$1.5 Mpc in comoving distance at $z = 2.5$. Our prescriptions also improve the accuracy of the best available multifeature redshift determination algorithm by $\sim$100 km s^{-1}, indicating that the spectroscopic properties of the C IV emission line can provide robust redshift estimates for high-redshift quasars. We discuss the prospects of our prescriptions for cosmological and quasar studies utilizing upcoming large spectroscopic surveys.

Unified Astronomy Thesaurus concepts: Quasars (1319); Surveys (1671); Active galactic nuclei (16)

Supporting material: machine-readable tables

1. Introduction

Obtaining systemic redshifts ($z_{\rm sys}$) for quasars to accuracies better than 1000 km s^{-1} is necessary for a variety of reasons. These include measuring the kinematics of outflowing material near the supermassive black hole that impact star formation rates in the quasar's host galaxy (e.g., Hopkins & Elvis 2010; Maiolino et al. 2012; Carniani et al. 2018) and cosmological studies that utilize redshifts as distance indicators, such as quasar clustering and the proximity effect at high redshift (e.g., Alcock & Paczynski 1979; Hogg 1999; Shen et al. 2007; Dawson et al. 2013; McGreer et al. 2016; Zhao et al. 2019).

A quasar $z_{\rm sys}$ value is typically determined from spectroscopy in the optical band relying, particularly, on the wavelength of the peak of the narrow [O III] λ5007 emission line at $z \lesssim 0.8$, the Mg II $\lambda\lambda$2798, 2803 doublet for $0.4 \lesssim z \lesssim 2.3$, or the Balmer lines up to $z \sim 1$ in order of increasing uncertainty on the derived $z_{\rm sys}$ value, ranging from $\sim$50 km s^{-1} to $\sim$600 km s^{-1} (e.g., Boroson 2005; Shen et al. 2016; Nguyen et al. 2020). However, at higher redshifts, these $z_{\rm sys}$ indicators shift out of the optical band, and redshift determinations usually rely on shorter wavelength and typically higher ionization emission lines such as C IV λ1549. Such emission lines are known to show additional kinematic offsets of up to several 10^3 km s^{-1} that add uncertainties of this magnitude to the derived redshift values (e.g., Gaskell 1982; Tytler & Fan 1992; Gibson et al. 2009; Shen et al. 2016; Vietri et al. 2018). The redshifts of distant quasars determined from large spectroscopic surveys (e.g., Sloan Digital Sky Survey, SDSS; York et al. 2000; DESI Collaboration et al. 2016; Tamura et al. 2016; Lyke et al. 2020), which are limited to $\lambda_{\rm obs} \lesssim 1$ μm, therefore will have uncertainties on the order of tens of Mpc at $z = 2.5$ when

converting from velocity space into comoving distance (e.g., Font-Ribera et al. 2013).

A direct comparison of SDSS pipeline redshifts (Bolton et al. 2012; Lyke et al. 2020) with $z_{\rm sys}$ values obtained from rest-frame optical indicators shows that corrections to UV-based redshifts can be made despite the presence of potentially large uncertainties. Past investigations such as Hewett & Wild (2010), Mason et al. (2017) and Dix et al. (2020), hereafter HW10, M17, and D20, respectively, have demonstrated that these uncertainties can be mitigated through corrections obtained from regression analyses based on preexisting rest-frame UV-optical spectral properties and used as prescriptions for correcting UV-based redshifts.

HW10 relied primarily on sampling methods wherein an average quasar spectrum was generated using a large sample of existing quasar spectra, and then statistical analysis was used to provide offsets for any given quasar with respect to this "master" spectrum in order to correct for any uncertainties. However, this offset correction becomes less reliable for high-redshift quasars as important emission lines such as [O III] and Mg II leave the optical band, and so additional corrections are needed (see, e.g., Rankine et al. 2020).

M17 and D20 used regression analyses that apply empirical corrections to UV-based redshifts involving the C IV spectroscopic parameter space, a diagnostic of quasar accretion power (Richards et al. 2011; Rivera et al. 2020; Rankine et al. 2020), which affects the wavelengths of emission-line peaks. Specifically, these parameters include the rest-frame equivalent width (EW) and FWHM intensity of the C IV line[16] as well as the continuum luminosity at the base of this line. Such corrections have been applied to sources that lack broad absorption lines (BALs) and are not radio loud[17] in order to minimize the effects of absorption and continuum boosting, respectively, to the C IV line profile to mitigate potential complications arising from these sources and provide the most reliable results possible.

The D20 analysis, an extension of the M17 study, was based on a nonuniform sample of 55 SDSS sources with spectral coverage in the rest-frame optical and UV. Here, we use a larger and more uniform sample of 121 sources with highly reliable $z_{\rm sys}$ values drawn from an augmentation of the Gemini Near Infrared Spectrograph–Distant Quasar Survey (GNIRS-DQS) near-infrared (NIR) spectral inventory (Matthews et al. 2021, hereafter M21). Our results allow us to obtain significantly improved prescriptions for correcting UV-based redshifts. Section 2 describes the properties of the quasar sample and the respective redshift measurements, along with an augmentation of the M21 catalog of spectral properties from GNIRS-DQS. Section 3 presents prescriptions for correcting UV-based quasar redshifts based on multiple regression analyses including several velocity width indicators, alongside discussion of the redshift dependence of the velocity offset corrections and redshift estimates for quasars with extremely high velocity offsets. Our conclusions are presented in Section 4. Throughout this paper, we adopt a flat ΛCDM cosmology with $\Omega_\Lambda = 1 - \Omega_{\rm M} = 0.7$ and $H_0 = 70$ km s^{-1} Mpc^{-1} (e.g., Spergel et al. 2007).

[16] We discuss additional velocity width measurement methods in Appendix.

[17] We consider radio-loud quasars to have $R > 100$, where R is defined as $R = f_\nu$(5 GHz) / f_ν (4400 Å) and where f_ν(5 GHz) and f_ν(4400 Å) are the flux densities at a rest-frame frequency of 5 GHz and a rest-frame wavelength of 4400 Å, respectively (Kellermann et al. 1989).

2. Sample Selection

Our quasar sample is drawn from GNIRS-DQS, which comprises the largest, most uniform sample of optically selected high-redshift quasars having NIR spectroscopic coverage (M21). The GNIRS-DQS sources were selected from all SDSS quasars (Pâris et al. 2018; Lyke et al. 2020) having $-28.0 \lesssim M_i \lesssim -30.0$ mag at $1.55 \lesssim z \lesssim 3.50$ for which the Hβ and [O III] emission lines can be covered in either the J, H, or K bands, spanning a monochromatic luminosity (λL_λ) at 5100 Å in the range of $\sim 10^{46}$–10^{47} erg s^{-1} Å^{-1}. We augment the original GNIRS-DQS sample with 34 additional sources, selected in a similar fashion as described below, and shown in Figure 1. Distributions of radio loudness and [O III] λ5007 EW for the GNIRS-DQS sources are shown in Figures 2 and 3, respectively.

2.1. The Augmented GNIRS-DQS Catalog

We present spectroscopic observations for 34 sources that were observed in semester 2020B as part of our GNIRS-DQS campaign (see M21 for a detailed description of the observational strategy and the instrument configuration). We also include spectroscopic observations for 11 sources that were observed in a similar fashion, albeit with a narrower slit, 0.″30, in semester 2015A (program GN-2015A-Q-68; PI: Brotherton). Three of the 2020B sources and one of the 2015A sources, were observed twice in their respective semesters. The log of these additional observations is given in Table 1.

Three of the 2020B observations were repeat observations of SDSS J094427.27+614424.6, SDSS J113924.64+332436.9, and SDSS J223934.45-004707.2, which were previously described in M21; the repeat observations were intended to improve the quality of the spectroscopic data for these three sources (see Table 1). Four of the 2020B observations, and four of the 2015A observations did not yield adequate spectroscopic data and are marked appropriately in Table 1. Therefore, in total, we have 37 useful observations, three of which are of sources that were already presented in M21. The augmented GNIRS-DQS catalog comprises of a total of 260 sources, 34 of which have been added in this work.

The formatting for the basic spectral properties of all 260 GNIRS-DQS objects is presented in Tables 2 and 3 in a similar fashion to Tables 2 and 3 in M21. The GNIRS-DQS sample was originally selected from the SDSS quasar catalogs for Data Release (DR) 12 and DR14 (Pâris et al. 2017, 2018); the augmented GNIRS-DQS catalog presented here includes 27 sources that were selected from SDSS DR16 (Lyke et al. 2020), which are marked appropriately in Table 1, and seven sources from GN-2015A-Q-68 that were selected from SDSS DR7 (Schneider et al. 2010). DR16 measurements have been adopted for the full sample (Lyke et al. 2020). Table 4 presents the parameters used to model all of the emission lines, using Gaussian profiles, in the GNIRS-DQS spectra. For each profile, these parameters include the observed-frame wavelength of the line peak, velocity width (FWHM), and flux-density normalization (f_λ). All of the GNIRS spectra and their best-fit models are available electronically at NOIRlab.[18]

2.2. Improved Spectroscopic Inventory

Tables 2 and 3 include improved measurements of all spectral features. In particular, they include measurements of the rest-

[18] https://datalab.noirlab.edu/gnirs_dqs.php

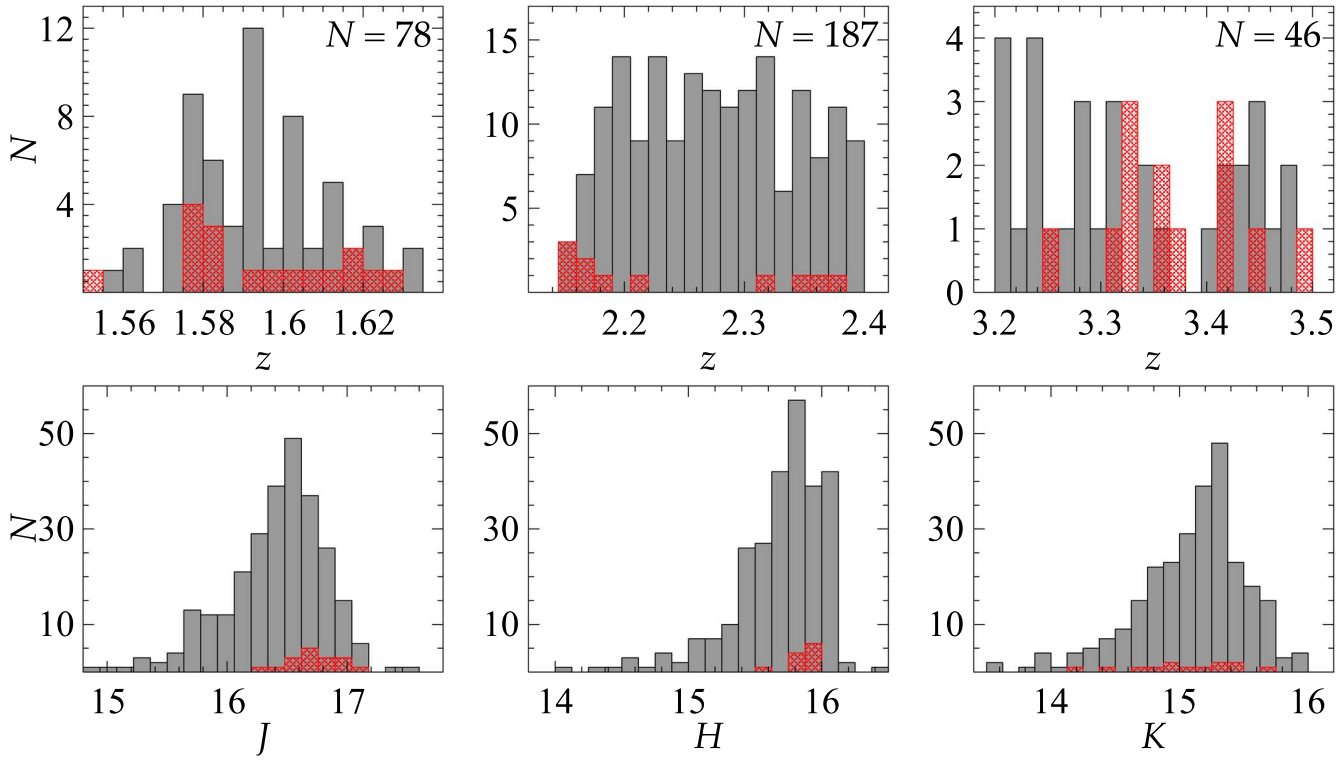

Figure 1. Distributions of the redshift estimate from SDSS (Lyke et al. 2020, Table D1, column 27 "Z") in each redshift interval (top row) and corresponding magnitude distributions (bottom row). The initial GNIRS-DQS sample is marked in gray, and sources from the augmented sample are shown in red. The three redshift bins correspond to the Hβ and [O III] lines appearing at the center of the J, H, or K photometric bands. The number of sources observed in each redshift bin is marked in each of the top panels. Of a total of 311 sources observed, 272 of which were reported in M21, usable NIR spectra were obtained for 260 sources (∼84% completion rate); the NIR spectra of 226 of these were presented in M21, and the remaining 34 are presented in this work.

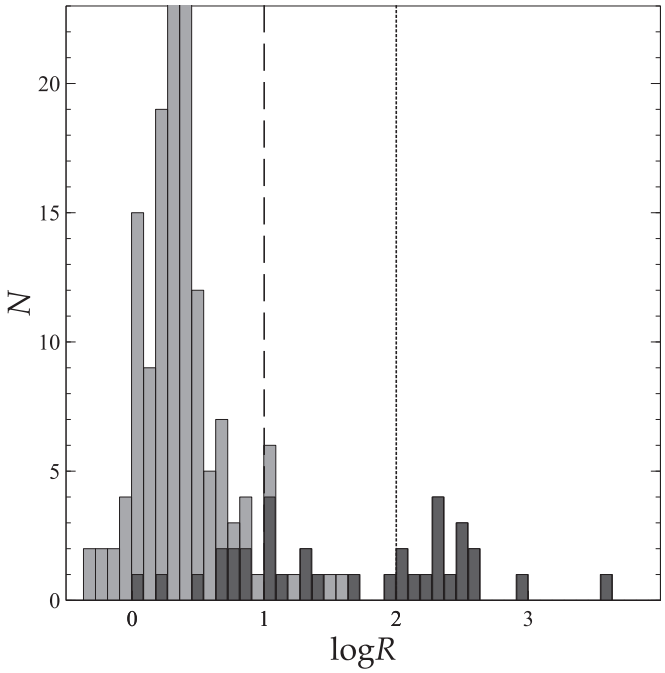

Figure 2. Radio-loudness distribution of the GNIRS-DQS sources. Darker shaded regions indicate new sources not in M21. The dashed line at log $R = 1$ indicates the threshold for radio-quiet quasars, and the dotted line at log $R = 2$ indicates the threshold for radio-loud quasars (see also M21).

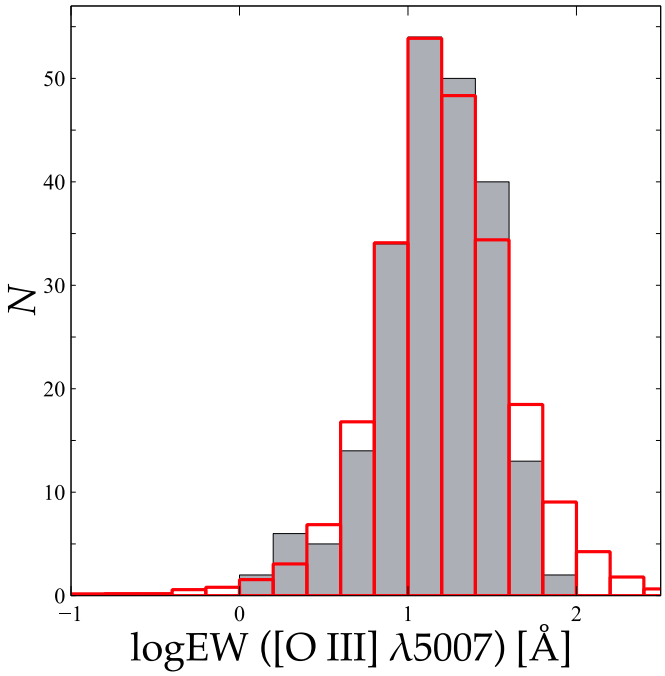

Figure 3. [O III] λ5007 rest-frame EW distribution of 220 GNIRS-DQS sources (solid gray histogram) and a similar distribution from Shen et al. (2011; red outline; scaled down by a factor of 500). See M21 for additional discussion. Forty sources did not meet our threshold of reliability for an [O III] EW measurement that we require to be greater than 1 Å.

frame optical Fe II emission blend that was fitted for each source in the same manner as in M21; however, each such feature now has a measured EW value and errors, thus effectively removing all the upper limits on the EWs (see Table 2 of M21). We fit two Gaussians to each broad emission-line profile to accommodate a possible asymmetry arising from, e.g., absorption or outflows. We

Table 1
GNIRS-DQS Observation Log

Quasar	z_{SDSS}[a]	J (mag)	H (mag)	K (mag)	Obs. Date	Net Exp. (s)	Comments	BAL	RL
(1)	(2)	(3)	(4)	(5)	(6)	(7)	(8)	(9)	(10)
SDSS J001018.88+280932.5[b]	1.612	16.56	15.80	15.76	2020 Dec 09	1800	…	…	…
SDSS J003001.11−015743.5	1.582	17.08	15.96	15.76	2020 Sep 09	1800	…	…	…
SDSS J003853.15+333044.3	2.357	16.81	15.98	15.29	2020 Dec 25	1800	…	…	…
SDSS J004613.54+010425.7	2.150	16.44	15.85	15.02	2020 Dec 11	1800	…	1	…
SDSS J004710.48+163106.5	2.165	16.33	15.62	14.90	2020 Dec 11	1800	…	…	…
SDSS J005307.71+191022.7[b]	1.583	16.72	15.79	15.43	2020 Sep 08	1800	…	…	…
SDSS J020329.86-091020.3[b]	1.579	17.02	15.97	15.64	2020 Aug 23	900	…	…	…
	…	…	…	…	2020 Sep 11	900	…	…	…
SDSS J073132.18+461347.0[b]	1.578	16.71	15.83	15.31	2020 Sep 29	1350	…	…	…
SDSS J080117.91+333411.9[b]	1.598	16.73	15.99	15.79	2020 Oct 05	1350	…	…	…
SDSS J080429.61+113013.9[b]	2.165	16.64	15.99	15.13	2020 Nov 27	1800	2	…	…
SDSS J080636.81+345048.5[b]	1.553	16.45	15.88	16.58	2020 Sep 30	1800	…	1	…
SDSS J080707.37+260729.1[b]	2.312	16.84	15.99	15.53	2020 Sep 30	1800	2	…	…
SDSS J081520.94+323512.9[b]	1.584	16.90	15.85	15.55	2020 Nov 28	1800	2	…	…
SDSS J084017.87+103428.8	3.330	16.69	16.47	15.27	2015 Apr 23	1720	…	…	…
SDSS J084401.95+050357.9	3.350	15.39	14.93	14.19	2015 Apr 06	800	…	…	…
SDSS J084526.75+550546.8[b]	1.620	16.33	15.65	15.18	2020 Nov 27	1800	…	…	…
SDSS J091425.72+504854.9[b]	2.341	17.18	15.98	15.17	2020 Nov 29	1800	…	…	…
SDSS J092942.97+064604.1[b]	1.608	16.65	15.53	15.28	2020 Nov 30	1800	…	…	…
SDSS J094140.16+325703.2[b]	3.452	16.55	15.81	15.24	2020 Nov 29	1800	…	…	…
SDSS J094427.27+614424.6[b]	2.340	16.41	15.61	14.72	2020 Dec 09	1800	3	…	…
SDSS J095047.45+194446.1[b]	1.575	16.80	15.98	15.62	2020 Dec 12	900	…	…	…
	…	…	…	…	2020 Dec 21	900	…	…	…
SDSS J095555.68+351652.6[b]	1.616	16.99	15.97	15.85	2020 Dec 09	1800	…	…	…
SDSS J101724.26+333403.3[b]	1.579	16.49	15.84	15.40	2020 Nov 30	1800	…	…	…
SDSS J111127.43+293319.3[b]	2.178	16.42	15.88	15.10	2020 Dec 31	1800	2	…	…
SDSS J112726.81+601020.2[b]	2.159	16.60	15.79	15.40	2020 Dec 31	2250	…	…	…
SDSS J112938.46+440325.0[b]	2.213	16.99	15.88	15.11	2021 Jan 02	1800	…	1	…
SDSS J113330.17+144758.8[b]	3.248	16.90	15.88	15.64	2021 Jan 02	1800	…	1	…
SDSS J113924.64+332436.9[b]	2.314	16.38	15.95	14.85	2020 Dec 09	1800	3	…	…
SDSS J122343.15+503753.4	3.491	15.90	15.57	14.69	2015 Mar 30	1160	…	…	…
SDSS J122938.61+462430.5[b]	2.152	16.30	15.77	15.19	2020 Nov 30	1800	…	…	…
SDSS J130213.54+084208.6	3.305	16.12	15.64	15.02	2015 Apr 01	1720	2	…	…
SDSS J131048.17+361557.7	3.420	15.79	15.11	14.38	2015 Apr 05	800	2	…	…
SDSS J132845.00+510225.8	3.411	16.10	15.53	14.77	2015 Apr 05	1160	…	…	…
SDSS J141321.05+092204.8	3.327	16.16	15.63	15.05	2015 Apr 05	1160	…	…	…
SDSS J142123.97+463318.0	3.378	16.28	15.49	14.89	2015 Apr 07	1700	2	…	…
SDSS J142755.85−002951.1	3.362	16.60	15.91	15.27	2015 Apr 01	1720	…	…	…
SDSS J165523.09+184708.4	3.327	16.28	15.88	15.19	2015 Apr 08	1720	2	…	…
SDSS J173352.23+540030.4	3.424	15.87	15.72	14.95	2015 Mar 23	1190	…	…	…
	…	…	…	…	2015 Apr 01	680	…	…	…
SDSS J210558.29−011127.5	1.625	16.61	15.49	15.54	2020 Aug 21	2250	1	…	…
SDSS J211251.06+000808.3[b]	1.618	16.85	15.89	15.89	2020 Aug 19	1800	1	…	…
SDSS J213655.35−080910.1	1.591	16.96	15.56	15.74	2020 Aug 23	1800	…	…	…
SDSS J220139.99+114140.8[b]	2.382	16.87	15.76	15.84	2020 Aug 30	1800	1	…	…
SDSS J222310.76+180308.1[b]	1.602	16.70	15.99	15.60	2020 Sep 01	1800	1	…	…
SDSS J223934.45−004707.2	2.121	16.91	15.97	15.70	2020 Oct 03	1800	1, 3	…	…
SDSS J233304.61−092710.9	2.121	16.17	15.41	14.83	2021 Jan 01	1800	1	…	…
	…	…	…	…	2021 Jan 02	900	…	…	…

Notes. Several sources have more than one observation, indicated by an empty source name. Only the 2020B and 2015A observations are shown. All 333 observations of GNIRS-DQS are available. All SDSS data are taken from DR16. Comments in Column (8) represent (1) at least one exposure did not meet our observation conditions requirements; (2) observation failed to provide spectrum of the source due to bad weather, instrument artifacts, or other technical difficulties during the observation; and (3) reobserved and updated from M21.

[a] Value based on best available measurement in SDSS DR16 (Lyke et al. 2020, Table D1, column 27 "Z").

[b] Denotes object selected from DR16.

(This table is available in machine-readable form.)

note that the two Gaussian fit per broad emission line is adopted only to characterize the line shape; the two Gaussians do not imply two physically distinct regions. The errors on the spectral measurements were calculated in the same manner as the other uncertainties described in M21, with upper and lower values being derived from a distribution of values recorded during the iterative process of broadening the Fe II template (see M21 for a detailed description of the Fe II blend fitting process).

In addition to the inclusion of 34 new sources, Tables 2 and 3 contain the most reliable data for the entire GNIRS-DQS sample following remeasurement of each spectrum with additional vetting and visual inspection, particularly with respect to the [O III] and Fe II fitting. These data therefore supersede the corresponding data presented in M21.

2.3. C IV Emission-line Measurements

M17 and D20 found that the accuracy and precision of a source's UV-based redshift can be significantly improved when regressed against the FWHM and EW of its C IV line as well as the UV continuum luminosity at a rest-frame wavelength of 1350 Å (L_{1350}).[19] The C IV emission line has been measured in the SDSS spectrum of each GNIRS-DQS source using the same fitting approach outlined in D20, which closely follows the methods utilized in both M21 and this work; the C IV emission-line properties of all the GNIRS-DQS sources appear in Dix et al. (2023), hereafter Paper II.

3. Correcting UV-based Redshifts

Our aim is to derive corrections that, on average, shift the velocity offsets of the UV-based redshifts as close as possible to a velocity offset of zero km s^{-1} from $z_{\rm sys}$ based on the [O III] λ5007 line. We derive this correction by applying a regression analysis to a calibration sample of 121 sources from GNIRS-DQS as described below.

The sample used for this analysis is a subset of the augmented GNIRS-DQS sample described in Section 2. Starting with the 260 GNIRS-DQS sources with useful NIR spectra, we include only the 220 objects with [O III] rest-frame EW measurements greater than 1 Å that can provide the most accurate values of $z_{\rm sys}$ (see Figure 3), i.e., 40 sources whose $z_{\rm sys}$ values were based on either Mg II or Hβ were removed. We then remove 52 BAL quasars, identified as such based on criteria outlined in their respective source catalogs using the "balnicity" index and visual inspection (see Gibson et al. 2009; Shen et al. 2011; Pâris et al. 2017, 2018; Lyke et al. 2020) as the BAL troughs often degrade measurements of the EW and FWHM for C IV, which are of primary importance for our regression analysis (e.g., Begelman et al. 1991; Gibson et al. 2009). We also remove 17 radio-loud (RL) quasars (having $R > 100$; see Figure 2), one of which, SDSS J114705.24+083900.6, is also classified as a BAL quasar, due to potential continuum boosting, which may affect both EW (C IV) and L_{1350} measurements (e.g., Miller et al. 2011).

Two additional sources, SDSS J073132.18+461347.0 and SDSS J141617.38+264906.1, were excluded due to the inability to measure the C IV line reliably (see Paper II). Finally, 29 objects were removed from the sample due to additional visual inspection and a lack of a prominent [O III] λ5007 emission line. The result of this selection process is a calibration sample of 121 sources, presented in Table 5, which is a representative sample of optically selected quasars (see Section 2) used to derive prescriptions for correcting UV-based redshifts through linear regression analysis.

The redshift corrections are performed on redshifts obtained using three separate techniques: (1) measurements of the observed-frame wavelength of the peak of the C IV emission line, (2) HW10 redshifts (P. Hewett 2022, private communication), and (3) SDSS Pipeline redshifts (Bolton et al. 2012, Table D1, column 29 "Z_PIPE"). The HW10 redshifts are notable as they already have a primary redshift correction applied.

The principal metric under investigation in this work is the initial velocity offset (Δv_i) between each of the aforementioned three UV-based redshifts ($z_{\rm meas}$) and the $z_{\rm sys}$ value of a source determined from its [O III] λ5007 emission line by measuring the line peak in each spectrum, which is presented in Table 2. This offset is computed using the following equation (see D20):

$$\Delta v_i = c\left(\frac{z_{\rm meas} - z_{\rm sys}}{1 + z_{\rm sys}}\right). \quad (1)$$

These initial velocity offset values are presented in Table 5 and are shown in the top panels of Figure 4.

As shown in Table 5, there is one source, SDSS J090247.57+304120.7, where the SDSS pipeline produces an erroneous redshift, resulting in an unrealistically high velocity offset of $|\Delta v_i| > 16{,}000$ km s^{-1}, while the velocity offsets for this source from the C IV and HW10 methods yield values that are only -170 and $+70$ km s^{-1}, respectively. As a result, this source is excluded from the SDSS pipeline analysis but is retained in the C IV and HW10 analyses.

It is known that the C IV velocity offsets are correlated with the C IV FWHM (e.g., Coatman et al. 2017). However, as was discovered by M17 and D20, additional corrections to the velocity offsets can be obtained by including two additional parameters: EW(C IV) and L_{1350}. In this work, we confirm that all three parameters, FWHM(C IV), EW(C IV), and L_{1350}, are required for obtaining the best corrections for the velocity offsets in the following manner:

$$\begin{aligned}\Delta v_{\rm corr}\ ({\rm km\ s^{-1}}) = {} & \alpha {\rm log FWHM}_{\rm C\ IV}\ ({\rm km\ s^{-1}}) \\ & + \beta {\rm log EW}_{\rm C\ IV}\ ({\rm \AA}) \\ & + \gamma \log L_{1350}\ (10^{-17}\ erg\ s^{-1}{\rm \AA}^{-1}), \end{aligned} \quad (2)$$

where $\Delta v_{\rm corr}$ is the velocity offset we subtract from the initial velocity offset calculated using Equation (1).

The final, post-correction velocity offset, $\Delta v_f = \Delta v_i - \Delta v_{\rm corr}$, is displayed in the bottom panels of Figure 4. Since the goal of Equation (2) is to eliminate the velocity offsets, then, by definition, the mean (μ) of $\Delta v_i - \Delta v_{\rm corr}$ is zero. This $\Delta v_{\rm corr}$ value is used to obtain a revised $z_{\rm sys}$ prediction by adjusting the initially measured redshift of a quasar. From Equation (1), solving for $z_{\rm meas}$, and substituting $z_{\rm meas} = z_{\rm sys}$ and $v_{\rm corr} = v_i$, we get

$$z_{\rm rev} = z_{\rm meas} + \frac{\Delta v_{\rm corr}(1 + z_{\rm meas})}{c}, \quad (3)$$

where $z_{\rm rev}$ is the revised, more accurate, and more precise redshift.

Starting with our 121-source calibration sample, we run linear regressions using the three parameters defined in Equation (2). The results provide the $\Delta v_{\rm corr}$ values from Equation (2) that are subtracted from the initial velocity offsets of the sources (from Table 5).

Distributions of the Δv_i and Δv_f values are plotted in the top and bottom panels in Figure 4, respectively. We observe that the C IV-based Δv_i values are skewed toward negative values (blueshifts) with a mean velocity offset of $\mu = -864$ km s^{-1} and a standard deviation of $\sigma = 804$ km s^{-1}. The SDSS pipeline-based Δv_i values have a considerably smaller negative

[19] Objects with redshifts $z < 1.65$ had L_{1350} values extrapolated from L_{3000} assuming a continuum power law of the form $f_\nu \propto \nu^{0.5}$ (e.g., Vanden Berk et al. 2001).

Table 2
Column Headings for Spectral Measurements

Column (1)	Name (2)	Bytes (3)	Format (4)	Units (5)	Description (6)
1	OBJ	(1–24)	A24	⋯	SDSS object designation
2	ZSYS	(26–30)	F5.3	⋯	Systemic redshifts
3	ZSRC	(32–34)	A3	⋯	Emission-line source for systemic redshift as described in M21
3	LC_MG II	(36–38)	I5	Å	Mg II observed-frame wavelength[a]
4	LC_MG II_UPP	(40–41)	I2	Å	Upper uncertainty for the line peak of Mg II
5	LC_MG II_LOW	(43–44)	I2	Å	Lower uncertainty for the line peak of Mg II
6	FWHM_MG II	(46–49)	I4	km s^{-1}	FWHM of Mg II
7	FWHM_MG II_UPP	(51–54)	I4	km s^{-1}	Upper uncertainty of FWHM of Mg II
8	FWHM_MG II_LOW	(56–59)	I4	km s^{-1}	Lower uncertainty of FWHM of Mg II
9	EW_MG II	(61–62)	I2	Å	Rest-frame EW of Mg II
10	EW_MG II_UPP	(64–65)	I2	Å	Upper uncertainty of EW of Mg II
11	EW_MG II_LOW	(67–68)	I2	Å	Lower uncertainty of EW of Mg II
12	AS_MG II	(70–78)	E9.2	⋯	Asymmetry of the double Gaussian fit profile of Mg II
13	KURT_MG II	(80–83)	F4.2	⋯	Kurtosis of the double Gaussian fit profile of Mg II
14	LC_HB	(85–89)	I5	Å	Hβ observed-frame wavelength[a]
15	LC_HB_UPP	(91–92)	I2	Å	Upper uncertainty for the line peak of Hβ
16	LC_HB_LOW	(94–95)	I2	Å	Lower uncertainty for the line peak of Hβ
17	FWHM_HB	(97–101)	I5	km s^{-1}	FWHM of Hβ
18	FWHM_HB_UPP	(103–107)	I5	km s^{-1}	Upper uncertainty of FWHM of Hβ
19	FWHM_HB_LOW	(109–112)	I5	km s^{-1}	Lower uncertainty of FWHM of Hβ
20	EW_HB	(114–116)	I3	Å	Rest-frame EW of Hβ
21	EW_HB_UPP	(118–119)	I2	Å	Upper uncertainty of EW of Hβ
22	EW_HB_LOW	(121–122)	I2	Å	Lower uncertainty of EW of Hβ
23	AS_HB	(124–132)	E9.2	⋯	Asymmetry of the double Gaussian fit profile of Hβ
24	KURT_HB	(134–137)	F4.2	⋯	Kurtosis of the double Gaussian fit profile of Hβ
25	LC_O III	(139–143)	I5	Å	[O III] λ5007 observed-frame wavelength[a]
26	LC_O III_UPP	(145–146)	I2	Å	Upper uncertainty for the line peak of [O III] λ5007
27	LC_O III_LOW	(148–149)	I2	Å	Lower uncertainty for the line peak of [O III] λ5007
28	FWHM_O III	(151–154)	I4	km s^{-1}	FWHM of [O III] λ5007
29	FWHM_O III_UPP	(156–159)	I4	km s^{-1}	Upper uncertainty of FWHM of [O III] λ5007
30	FWHM_O III_LOW	(161–164)	I4	km s^{-1}	Lower uncertainty of FWHM of [O III] λ5007
31	EW_O III	(166–173)	E8.2	Å	Rest-frame EW of [O III] λ5007
32	EW_O III_UPP	(175–182)	E8.2	Å	Upper uncertainty of EW of [O III] λ5007
33	EW_O III_LOW	(184–191)	E8.2	Å	Lower uncertainty of EW of [O III] λ5007
34	AS_O III	(193–201)	E9.2	⋯	Asymmetry of the double Gaussian fit profile of [O III] λ5007
35	KURT_O III	(203–206)	F4.2	⋯	Kurtosis of the double Gaussian fit profile of [O III] λ5007
36	LC_HA	(208–212)	I5	Å	Hα observed-frame wavelength[a]
37	LC_HA_UPP	(214–215)	I2	Å	Upper uncertainty for the line peak of Hα
38	LC_HA_LOW	(217–218)	I2	Å	Lower uncertainty for the line peak of Hα
39	FWHM_HA	(220–223)	I4	km s^{-1}	FWHM of Hα
40	FWHM_HA_UPP	(225–228)	I4	km s^{-1}	Upper uncertainty of FWHM of Hα
41	FWHM_HA_LOW	(230–233)	I4	km s^{-1}	Lower uncertainty of FWHM of Hα
42	EW_HA	(235–237)	I3	Å	Rest-frame EW of Hα
43	EW_HA_UPP	(239–240)	I2	Å	Upper uncertainty of EW of Hα
44	EW_HA_LOW	(242–243)	I2	Å	Lower uncertainty of EW of Hα
45	AS_HA	(245–253)	E9.2	⋯	Asymmetry of the double Gaussian fit profile of Hα
46	KURT_HA	(255–258)	F4.2	⋯	Kurtosis of the double Gaussian fit profile of Hα
47	FWHM_FE II	(260–264)	F5.0	km s^{-1}	FWHM of the kernel Gaussian used to broaden the Fe II template
48	EW_FE II	(266–273)	E8.2	Å	Rest-frame EW of optical band Fe II as defined by Boroson & Green (1992)
49	EW_FE II_UPP	(275–282)	E8.2	Å	Upper uncertainty of EW of Fe II
50	EW_FE II_LOW	(284–291)	E8.2	Å	Lower uncertainty of EW of Fe II
51	LOGFλ5100	(293–298)	F6.2	erg s^{-1} cm^{-2} $Å^{-1}$	Flux density at rest-frame 5100 Å
52	LOGL5100	(300–304)	F5.2	erg s^{-1} $Å^{-1}$	Monochromatic luminosity at rest-frame 5100 Å based on z_{sys}

Note. Data formatting used for the catalog. Asymmetry is defined here as the skewness of the Gaussian fits, i.e., a measure of the asymmetry of the distribution about its mean, $s = E(x-\mu)^3/\sigma^3$, where μ is the mean of x, σ is the standard deviation of x, and $E(t)$ is the expectation value. Kurtosis is the quantification of the "tails" of the Gaussian fits defined as $k = E(x-\mu)^4/\sigma^4$. All of the GNIRS spectra and their best-fit models are available electronically at: https://datalab.noirlab.edu/gnirs_dqs.php.

[a] The emission-line peak based on the peak-fit value.

(This table is available in its entirety in machine-readable form.)

Table 3
Column Headings for Supplemental Emission-line Measurements

Column (1)	Name (2)	Bytes (3)	Format (4)	Units (5)	Description (6)
1	OBJ	(1–24)	A24	⋯	SDSS object designation
2	LC_HD	(26–30)	I5	Å	Hδ observed-frame wavelength[a]
3	LC_HD_UPP	(32–33)	I2	Å	Upper uncertainty for the line peak of Hδ
4	LC_HD_LOW	(35–36)	I2	Å	Lower uncertainty for the line peak of Hδ
5	FWHM_HD	(38–41)	I4	km s^{-1}	FWHM of Hδ
6	FWHM_HD_UPP	(43–45)	I3	km s^{-1}	Upper uncertainty of FWHM of Hδ
7	FWHM_HD_LOW	(47–49)	I3	km s^{-1}	Lower uncertainty of FWHM of Hδ
8	EW_HD	(51–52)	I2	Å	Rest-frame EW of Hδ
9	EW_HD_UPP	(54–55)	I2	Å	Upper uncertainty of EW of Hδ
10	EW_HD_LOW	(57–58)	I2	Å	Lower uncertainty of EW of Hδ
11	AS_HD	(60–68)	E9.2	⋯	Asymmetry of the double Gaussian fit profile of Hδ
12	KURT_HD	(70–73)	F4.2	⋯	Kurtosis of the double Gaussian fit profile of Hδ
13	LC_HG	(75–79)	I5	Å	Hγ observed-frame wavelength[a]
14	LC_HG_UPP	(81–82)	I2	Å	Upper uncertainty for the line peak of Hγ
15	LC_HG_LOW	(84–85)	I2	Å	Lower uncertainty for the line peak of Hγ
16	FWHM_HG	(87–90)	I4	km s^{-1}	FWHM of Hγ
17	FWHM_HG_UPP	(92–95)	I4	km s^{-1}	Upper uncertainty of FWHM of Hγ
18	FWHM_HG_LOW	(97–100)	I4	km s^{-1}	Lower uncertainty of FWHM of Hγ
19	EW_HG	(102–103)	I2	Å	Rest-frame EW of Hγ
20	EW_HG_UPP	(105–106)	I2	Å	Upper uncertainty of EW of Hγ
21	EW_HG_LOW	(108–109)	I2	Å	Lower uncertainty of EW of Hγ
22	AS_HG	(111–119)	E9.2	⋯	Asymmetry of the double Gaussian fit profile of Hγ
23	KURT_HG	(121–124)	F4.2	⋯	Kurtosis of the double Gaussian fit profile of Hγ
24	LC_O II[b]	(126–130)	I5	Å	[O II] observed-frame wavelength[a]
25	LC_O II_UPP	(132–133)	I2	Å	Upper uncertainty for the line peak of [O II]
26	LC_O II_LOW	(135–136)	I2	Å	Lower uncertainty for the line peak of [O II]
27	FWHM_O II	(138–141)	I4	km s^{-1}	FWHM of [O II]
28	FWHM_O II_UPP	(143–147)	I5	km s^{-1}	Upper uncertainty of FWHM of [O II]
29	FWHM_O II_LOW	(149–152)	I4	km s^{-1}	Lower uncertainty of FWHM of [O II]
30	EW_O II	(154–155)	I2	Å	Rest-frame EW of [O II]
31	EW_O II_UPP	(157–158)	I2	Å	Upper uncertainty of EW of [O II]
32	EW_O II_LOW	(160–161)	I2	Å	Lower uncertainty of EW of [O II]
33	AS_O II	(163–171)	E9.2	⋯	Asymmetry of the double Gaussian fit profile of [O II]
34	KURT_O II	(173–176)	F4.2	⋯	Kurtosis of the double Gaussian fit profile of [O II]
35	LC_NE III[c]	(178–182)	I5	Å	[Ne III] observed-frame wavelength[a]
36	LC_NE III_UPP	(184–185)	I2	Å	Upper uncertainty for the line peak of [Ne III]
37	LC_NE III_LOW	(187–188)	I2	Å	Lower uncertainty for the line peak of [Ne III]
38	FWHM_NE III	(190–193)	I4	km s^{-1}	FWHM of [Ne III]
39	FWHM_NE III_UPP	(195–198)	I4	km s^{-1}	Upper uncertainty of FWHM of [Ne III]
40	FWHM_NE III_LOW	(200–203)	I4	km s^{-1}	Lower uncertainty of FWHM of [Ne III]
41	EW_NE III	(205–206)	I2	Å	Rest-frame EW of [Ne III]
42	EW_NE III_UPP	(208–209)	I2	Å	Upper uncertainty of EW of [Ne III]
43	EW_NE III_LOW	(211–212)	I2	Å	Lower uncertainty of EW of [Ne III]
44	AS_NE III	(214–222)	E9.2	⋯	Asymmetry of the double Gaussian fit profile of [Ne III]
45	KURT_NE III	(224–227)	F4.2	⋯	Kurtosis of the double Gaussian fit profile of [Ne III]

Notes. Data formatting used for the supplemental measurements in the supplemental features catalog.
[a] The emission-line peak based on the peak-fit value.
[b] [O II] λ 3727.
[c] [Ne III] λ 3870.

(This table is available in its entirety in machine-readable form.)

initial velocity offset of $\mu = -443$ km s^{-1} yet a larger standard deviation of $\sigma = 883$ km s^{-1}. As expected, the HW10-based Δv_i values show a mean initial velocity offset much closer to zero ($\mu = 92$ km s^{-1}), with the standard deviation being notably smaller than that of the C IV-based Δv_i values ($\sigma = 679$ km s^{-1}). Despite the improvements demonstrated by the HW10-based values, we are able to use our regression analysis to improve on UV-based redshift determinations further, as shown below.

As explained above, our redshift corrections yield mean Δv_f values of 0 km s^{-1} using all three UV-based methods (see the bottom panels of Figure 4). The standard deviations (σ) of the Δv_f values, on the other hand, are reduced by ∼18%, ∼2%, and ∼7% for the C IV, HW10, and SDSS pipeline methods, respectively, with respect to the measured Δv_i values. The median velocity offsets are also reduced significantly for all three methods. The linear regression coefficients (Equation (2)) used to achieve these corrections are presented in Table 6. The uncertainties on the

Table 4
Column Headings for Gaussian Parameters of Emission-line Profiles

Column (1)	Name (2)	Bytes (3)	Format (4)	Units (5)	Description (6)
1	OBJ	(1–24)	A24	…	SDSS object designation
2	MG II_LAM_PEAK_NARROW	(26–29)	I4	Å	Narrow Mg II peak[a]
3	MG II_STD_NARROW	(31–32)	I2	Å	Narrow Mg II width
4	MG II_F_LAM_NARROW	(34–37)	I4	erg s^{-1} cm^{-2} $Å^{-1}$	Narrow Mg II normalization
5	MG II_LAM_PEAK_BROAD	(39–42)	I4	Å	Broad Mg II peak[a]
6	MG II_STD_BROAD	(44–47)	I4	Å	Broad Mg II width
7	MG II_F_LAM_BROAD	(49–52)	I4	erg s^{-1} cm^{-2} $Å^{-1}$	Broad Mg II normalization
8	O II_LAM_PEAK_NARROW	(54–57)	I4	Å	Narrow [O II] peak[a]
9	O II_STD_NARROW	(59–60)	I2	Å	Narrow [O II] width
10	O II_F_LAM_NARROW	(62–65)	I4	erg s^{-1} cm^{-2} $Å^{-1}$	Narrow [O II] normalization
11	O II_LAM_PEAK_BROAD	(67–70)	I4	Å	Broad [O II] peak[a]
12	O II_STD_BROAD	(72–75)	I4	Å	Broad [O II] width
13	O II_F_LAM_BROAD	(77–78)	I2	erg s^{-1} cm^{-2} $Å^{-1}$	Broad [O II] normalization
14	NE III_LAM_PEAK_NARROW	(80–83)	I4	Å	Narrow [Ne III] peak[a]
15	NE III_STD_NARROW	(85–86)	I2	Å	Narrow [Ne III] width
16	NE III_F_LAM_NARROW	(88–89)	I2	erg s^{-1} cm^{-2} $Å^{-1}$	Narrow [Ne III] normalization
17	NE III_LAM_PEAK_BROAD	(91–94)	I4	Å	Broad [Ne III] peak[a]
18	NE III_STD_BROAD	(96–99)	I4	Å	Broad [Ne III] width
19	NE III_F_LAM_BROAD	(101–102)	I2	erg s^{-1} cm^{-2} $Å^{-1}$	Broad [Ne III] normalization
20	HD_LAM_PEAK_NARROW	(104–107)	I4	Å	Narrow Hδ peak[a]
21	HD_STD_NARROW	(109–110)	I2	Å	Narrow Hδ width
22	HD_F_LAM_NARROW	(112–113)	I2	erg s^{-1} cm^{-2} $Å^{-1}$	Narrow Hδ normalization
23	HD_LAM_PEAK_BROAD	(115–118)	I4	Å	Broad Hδpeak[a]
24	HD_STD_BROAD	(120–123)	I4	Å	Broad Hδ width
25	HD_F_LAM_BROAD	(125–127)	I3	erg s^{-1} cm^{-2} $Å^{-1}$	Broad Hδ normalization
26	HG_LAM_PEAK_NARROW	(129–132)	I4	Å	Narrow Hγ peak[a]
27	HG_STD_NARROW	(134–135)	I2	Å	Narrow Hγ width
28	HG_F_LAM_NARROW	(137–139)	I3	erg s^{-1} cm^{-2} $Å^{-1}$	Narrow Hγ normalization
29	HG_LAM_PEAK_BROAD	(141–144)	I4	Å	Broad Hγ peak[a]
30	HG_STD_BROAD	(146–149)	I4	Å	Broad Hγ width
31	HG_F_LAM_BROAD	(151–153)	I3	erg s^{-1} cm^{-2} $Å^{-1}$	Broad Hγ normalization
32	HB_LAM_PEAK_NARROW	(155–158)	I4	Å	Narrow Hβ peak[a]
33	HB_STD_NARROW	(160–162)	I3	Å	Narrow Hβ width
34	HB_F_LAM_NARROW	(164–166)	I3	erg s^{-1} cm^{-2} $Å^{-1}$	Narrow Hβ normalization
35	HB_LAM_PEAK_BROAD	(168–171)	I4	Å	Narrow Hβ peak[a]
36	HB_STD_BROAD	(173–175)	I3	Å	Broad Hβ width
37	HB_F_LAM_BROAD	(177–179)	I3	erg s^{-1} cm^{-2} $Å^{-1}$	Broad Hβ normalization
38	O III_1_LAM_PEAK_NARROW	(181–184)	I4	Å	Narrow [O III] 4959 Å peak[a]
39	O III_1_STD_NARROW	(186–187)	I2	Å	Narrow [O III] 4959 Å width
40	O III_1_F_LAM_NARROW	(189–191)	I3	erg s^{-1} cm^{-2} $Å^{-1}$	Narrow [O III] 4959 Å normalization
41	O III_1_LAM_PEAK_BROAD	(193–196)	I4	Å	Broad [O III] 4959 Å peak[a]
42	O III_1_STD_BROAD	(198–200)	I3	Å	Broad [O III] 4959 Å width
43	O III_1_F_LAM_BROAD	(202–204)	I3	erg s^{-1} cm^{-2} $Å^{-1}$	Broad [O III] 4959 Å normalization
44	O III_2_LAM_PEAK_NARROW	(206–209)	I4	Å	Narrow [O III] 5007 Å peak[a]
45	O III_2_STD_NARROW	(211–212)	I2	Å	Narrow[O III] 5007 Å width
46	O III_2_F_LAM_NARROW	(214–216)	I3	erg s^{-1} cm^{-2} $Å^{-1}$	Narrow [O III] 5007 Å normalization
47	O III_2_LAM_PEAK_BROAD	(218–221)	I4	Å	Broad [O III] 5007 Å peak[a]
48	O III_2_STD_BROAD	(223–225)	I3	Å	Broad [O III] 5007 Å width
49	O III_2_F_LAM_BROAD	(227–229)	I3	erg s^{-1} cm^{-2} $Å^{-1}$	Broad [O III] 5007 Å normalization
50	HA_LAM_PEAK_NARROW	(231–234)	I4	Å	Narrow Hα peak[a]
51	HA_STD_NARROW	(236–238)	I3	Å	Narrow Hα width
52	HA_F_LAM_NARROW	(240–243)	I4	erg s^{-1} cm^{-2} $Å^{-1}$	Narrow Hα normalization
53	HA_LAM_PEAK_BROAD	(245–248)	I4	Å	Broad Hα peak[a]
54	HA_STD_BROAD	(250–252)	I3	Å	Broad Hα width
55	HA_F_LAM_BROAD	(254–256)	I3	erg s^{-1} cm^{-2} $Å^{-1}$	Broad Hαnormalization

Note. Independent Gaussian-feature fit parameters for each emission line that was fit with both a narrow and broad Gaussian profile.
[a] The Gaussian profile peak based on the peak-fit value.

(This table is available in its entirety in machine-readable form.)

coefficients, shown in Table 6, from the regression defined in Equation (2) stem directly from the mean-squared error from the linear fit. These uncertainties (translated to ∼700 km s^{-1} in velocity space; see Figure 4) are considerably larger than the intrinsic uncertainties associated with the [O III] line wavelength calibration (on the order of ∼10 km s^{-1}; see M21) or the deviation of the

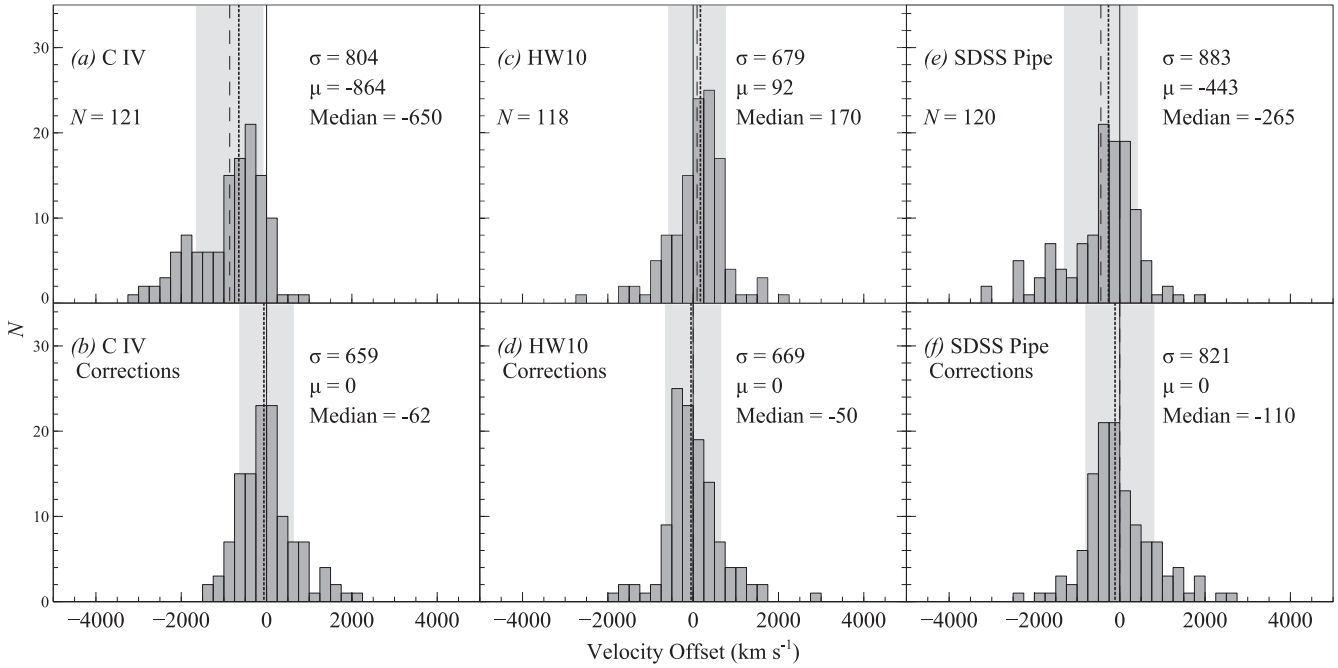

Figure 4. Velocity offsets relative to z_{sys} before (panels (a), (c), and (e)) and after (panels (b), (d), and (f)) the corrections using the linear regression coefficients given in Table 6. The standard deviation (shaded region), mean (dashed line), median (dotted line), and zero velocity offset (solid line) are marked in each panel. SDSS J090247.57+304120.7 does not appear on the SDSS Pipe panels due to its erroneous redshift. The mean (μ), median, and standard deviation (σ) given in units of km s^{-1}, are noted in each panel. The number of sources used in each regression analysis (N) is given in the upper panels.

Table 5
Redshifts and Velocity Offsets

Quasar	z_{sys} [a]	$z_{C\ IV}$ [b]	Δv_i (km s^{-1})	z_{HW10} [c]	Δv_i (km s^{-1})	z_{Pipe} [d]	Δv_i (km s^{-1})
SDSS J001018.88+280932.5	1.613	1.611	−230	⋯	⋯	1.612	−110
SDSS J001453.20+091217.6	2.340	2.326	−1250	2.344	340	2.308	−2840
SDSS J001914.46+155555.9	2.267	2.263	−370	2.276	830	2.271	350
SDSS J002634.46+274015.5	2.247	2.243	−340	2.247	50	2.267	1850
SDSS J003001.11−015743.5	1.588	1.579	−1030	1.590	200	1.582	−710
SDSS J003416.61+002241.1	1.631	1.626	−560	1.630	−50	1.627	−410
SDSS J004710.48+163106.5	2.192	2.162	−2770	⋯	⋯	2.165	−2490
SDSS J004719.71+014813.9	1.591	1.588	−340	1.590	−130	1.590	−130
SDSS J005233.67+014040.8	2.309	2.295	−1250	2.305	−370	2.291	−1620
SDSS J005307.71+191022.7	1.598	1.581	−1940	1.585	−1460	1.583	−1680

Notes. Complete table of 121 sources appears in the electronic version.
[a] Redshifts determined from the [O III] λ_{peak} as described in M21.
[b] Redshifts determined from the C IV λ_{peak} values given in Paper II.
[c] Acquired from HW10 and/or from P. Hewett (2022, private communication).
[d] Acquired from Lyke et al. (2020).

(This table is available in its entirety in machine-readable form.)

[O III] line from the systemic redshift (−48 km s^{-1} systematic offset and 56 km s^{-1} uncertainty; Shen et al. 2016); therefore, we adopt the regression uncertainties as the most conservative error estimates. Table 6 also gives the t value (e.g., Sheskin 2007) for confidence statistics in determining the importance of each parameter (see also D20), where t values of $|t| \gtrsim 2$ denote a strong correlation, with decreasing confidence as $t \to 0$.

Residuals of the 121-source sample both before and after our corrections are applied are presented in Figure 5. The residual distributions show the substantial reduction in the velocity offsets before and after each correction. The corrected velocity offsets for both the C IV and HW10-based methods are closer to zero than the corrected velocity offsets for the SDSS Pipeline method.

The relatively small improvement in the mean velocity offset (μ), and the standard deviation (σ), achieved for the HW10 method is likely related to the fact that our analysis constitutes a second-order correction to the one already employed by HW10; this result reinforces the general reliability of that method. The C IV-based redshifts, while based solely on a single emission line, provide a slightly smaller standard deviation than the HW10-based method when corrected using our regression analysis (see Figure 4). Finally, the SDSS Pipeline-based redshifts provide the least reliable results; in particular, we find that the SDSS Pipeline fails to produce a meaningful redshift for one out of 121 sources in our calibration sample (SDSS J090247.57+304120.7). Furthermore, DR16 redshifts (Lyke et al. 2020, Table D1, column 10

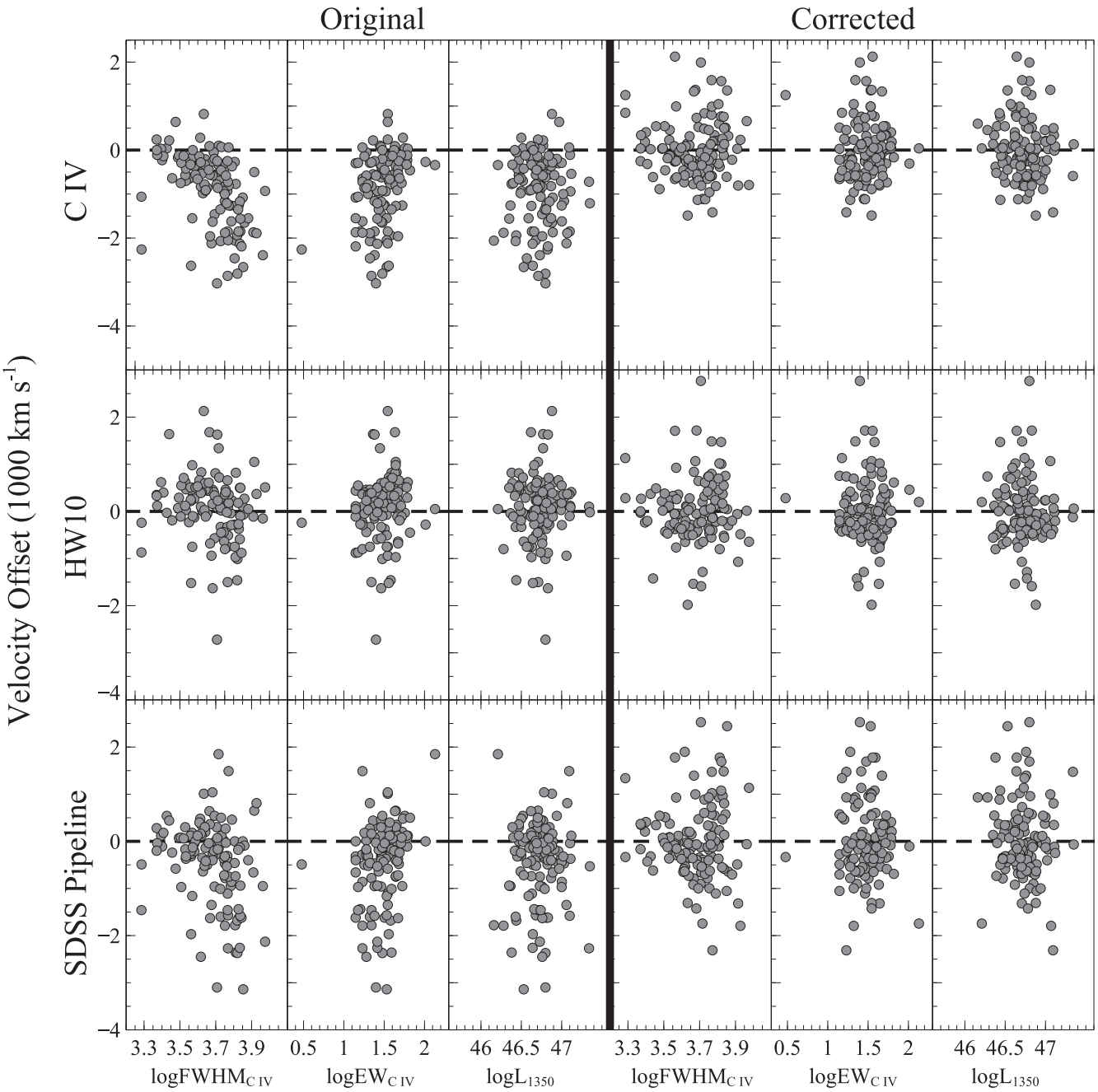

Figure 5. Residual velocity offsets with respect to z_{sys} before (three leftmost columns), and after (three rightmost columns), corrections are applied (see Equation (2)) against our regression parameters. SDSS J090247.57+304120.7 does not appear in the SDSS Pipeline panels due to its erroneously reported redshift, as discussed in Section 3.

"Z_QN") available for 101 sources from our sample provide significantly larger standard deviations than the SDSS Pipeline values both before and after the correction.

For our calibration sample, the largest Δv_i value is on the order of ~ -3000 km s^{-1}, with a few sources having velocity offsets within the $-3000\,\mathrm{km\ s^{-1}} \lesssim \Delta v_i \lesssim -2000\,\mathrm{km\ s^{-1}}$ range. Values of this magnitude, while high, are not unexpected due to the kinematics associated with luminous, rapidly accreting quasars that can directly affect the C IV emission line and cause large blueshifts (e.g., Murray et al. 1995; Sulentic et al. 2007; Shen et al. 2008; Dix et al. 2020). Panel (*a*) of Figure 4, and to a lesser extent panel (*e*), demonstrate the impact of this effect via the asymmetric distribution caused by this large range of velocity offsets. Nevertheless, our method tends to correct even these large velocity offsets to more reasonable values as shown in Figures 4 and 6.

Our velocity offset distributions may appear more asymmetric with respect to previous studies of this kind. For example, Shen et al. (Shen et al. 2011), who derived C IV velocity offsets based on Mg II (from the same SDSS spectrum), provide more symmetric distributions than those presented in Figure 4. This may be a result of the much larger uncertainties in the determination of z_{sys} from Mg II that was used in that study, compared with the uncertainties associated with the [O III] lines, which are up to an order of magnitude smaller (e.g., M21).

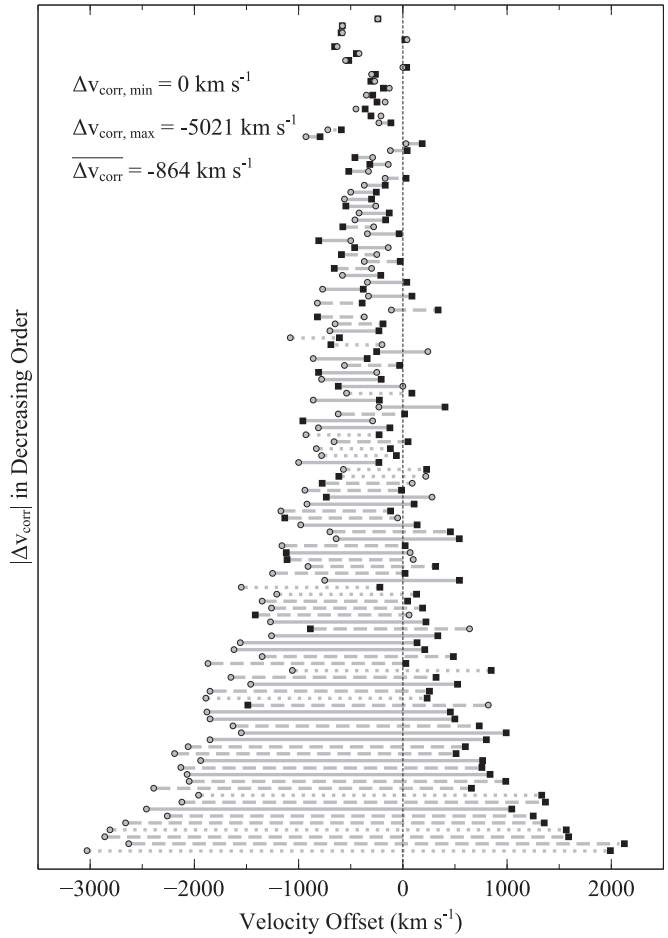

Figure 6. Initial velocity offsets (Δv_i; circles) compared to final velocity offsets (Δv_f; squares) for C IV-based redshifts of the calibration sample of 121 sources. The lines connecting the initial and final velocity offsets are sorted from top to bottom by the absolute value of the velocity offset correction ($|\Delta v_{corr}|$). Solid lines, dashed lines, and dotted lines refer to the following luminosity ranges: $46.08 < \log(L_{5100}) < 46.41$, $46.42 < \log(L_{5100}) < 46.74$, and $46.75 < \log(L_{5100}) < 47.09$, respectively. Fifteen sources have $|\Delta v_{corr}| < 100$ km s^{-1}, 11, three, and one of which belong to the lowest, medium, and highest luminosity ranges, respectively. While the majority of the Δv_i values, which are blueshifts, produce Δv_f values with the opposite sign, we also see Δv_i values which are redshifts that end up as blueshifts; however the overall effect of our regression analysis brings Δv_f values closer to zero. We find no trend between $|\Delta v_{corr}|$ and the monochromatic luminosity at rest-frame 5100 Å.

Table 6
Linear Regression Coefficients

UV-based Redshift Method (1)	Sample Size (2)	Regression Coefficients (3)	Value (4)	Error (5)	*t*-Value (6)
C IV	121	α	−2589	428	−6.05
		β	1156	292	3.95
		γ	148	36	4.15
HW10	118	α	−587	389	−1.51
		β	283	261	1.09
		γ	39	32	1.21
SDSS Pipe	120	α	9371	8557	1.10
		β	−3694	5851	−0.63
		γ	−655	715	−0.92

(This table is available in machine-readable form.)

The results of our regression analysis, presented in Table 6, provide considerably improved redshifts over the regression coefficients used by D20. When we employ the D20 regression coefficients on our calibration sample of 121 sources, we obtain standard deviations for the distributions of Δv_f which are ∼18% larger for the HW10 method, ∼32% larger for the SDSS Pipeline method, and ∼4% larger for the C IV-based redshifts compared to using the coefficients from Table 6. In summary, considering the four basic observables associated with the C IV emission line, one can derive the most accurate and precise prediction of the systemic redshift of a quasar using that sole emission line.

3.1. Redshift and Luminosity Dependence

Typically, redshifts are determined either spectroscopically or photometrically from multiple features (i.e., HW10 and the SDSS Pipeline). When some of these features are no longer available in a spectrum, our ability to determine the redshift is affected, and it is plausible that the initial velocity offsets depend also on source redshift. We search for such a dependence in our data by splitting our calibration sample into three redshift bins: $1.55 \lesssim z \lesssim 1.65$ (Bin 1), $2.10 \lesssim z \lesssim 2.40$ (Bin 2), and $3.20 \lesssim z \lesssim 3.50$ (Bin 3), which contain 37, 71, and 13 sources, respectively. These intervals ensure coverage of the [O III] λ5007 emission line in the *J*, *H*, or *K* bands, respectively (see Section 2).

We perform the regression analysis as described in Section 3 on each redshift bin separately. The results are presented in Table 7, and shown in Figure 7. The σ values of the velocity offsets across all redshift bins are roughly at or below the respective values in the bulk sample with respect to the C IV and HW10 methods (see Figure 4). Specifically, while the improvement in σ for the bulk sample considering the C IV-based method is ∼18%, we observe improvements of ∼9% in Bin 1, ∼25% in Bin 2, and ∼30% in Bin 3. Although the statistics in Bin 3 are limited, this trend may follow from the fact that the highest redshift bin tends to have higher luminosity quasars, which results in larger C IV blueshifts (e.g., due to outflows or winds) on average for more distant sources (e.g., Richards et al. 2011). Since our regression analysis relies heavily on the C IV parameter space, it is not unexpected that our corrections to the C IV-based redshifts would be more important for the more powerful sources found preferentially at higher redshifts.

Concerning the HW10-based method, our corrections produce improvements in standard deviation ranging from ∼1% to ∼4%, with no apparent trend with redshift. Therefore, it seems that these improvements are not very sensitive to the coverage of the Mg II line, which is absent from Bin 3. This result may be indicative of the overall robustness of the HW10 method, as found from the entire sample (see Section 3 and Figure 4). Mild improvements, and no significant redshift dependence, are observed for the SDSS pipeline method, and the overall standard deviations of velocity offset distributions stemming from this method remain high (∼780 km s^{-1}) in Bins 2 and 3.

In general, the greatest limitation in our ability to search for a redshift dependence is the disparity in the number of sources in each bin as is also portrayed by the large uncertainties on the regression coefficients in Table 7. Therefore, we derived the Δv_{corr} values in each redshift bin using the coefficients from Table 6 and found that the standard deviations on the distributions, when compared to those presented in Figure 7,

Table 7
Linear Regression Coefficients for each Redshift Bin

UV-based Redshift Method (1)	Redshift Bin[a] (2)	Regression Coefficients (3)	Value (4)	Error (5)	t value (6)	Number of Sources (7)
		α	−1103	762	−1.45	
	1	β	1022	436	2.35	37
		γ	37	60	0.62	
		α	−3382	561	−6.02	
C IV	2	β	1357	441	3.08	71
		γ	204	48	4.21	
		α	−4802	1751	−2.74	
	3	β	−994	1234	−0.81	13
		γ	391	167	2.34	
		α	−467	641	−0.73	
	1	β	−29	359	−0.08	36
		γ	35	50	0.71	
		α	−758	532	−1.42	
HW10	2	β	717	415	1.73	70
		γ	41	46	0.89	
		α	−27	1571	−0.02	
	3	β	85	979	0.09	12
		γ	2	148	0.01	
		α	−251	780	−0.32	
	1	β	149	440	0.34	36
		γ	10	61	0.17	
		α	−2661	681	−3.91	
SDSS Pipe	2	β	1825	535	3.41	71
		γ	140	59	2.38	
		α	6314	2670	2.36	
	3	β	4486	1881	2.38	13
		γ	−643	255	−2.52	

Note.
[a] Bins 1, 2, and 3 correspond to redshift ranges of $1.55 \lesssim z \lesssim 1.65$, $2.10 \lesssim z \lesssim 2.40$, and $3.20 \lesssim z \lesssim 3.50$.
(This table is available in machine-readable form.)

are roughly consistent across all redshift bins (within ∼5%), which indicates no discernible redshift evolution in our sample. A significantly larger sample size, particularly in Bin 3 ($z \sim 3$), may allow for a more definitive conclusion in this matter. This highest redshift bin is particularly important given the absence of the Mg II lines from the optical spectrum and the need to reliably estimate redshifts of more distant sources.

In addition to exploring a possible redshift dependence, we also look to see if our ability to predict a quasar's z_{sys} value depends on source luminosity. We trisect the calibration sample into three L_{5100} ranges with roughly equal widths: 46.08–46.41, 46.42–46.74, and 46.75–47.09 and look for any significant statistical deviations with respect to the entire sample. The results are shown in Figure 6. We find that there appears to be no clear dependence on source luminosity. A possible explanation for this result is that our sample is flux limited, and therefore it is difficult to disentangle the strong redshift-luminosity dependence.

4. Summary and Conclusions

We present an augmented catalog of spectroscopic properties obtained from NIR observations of a uniform, flux-limited sample of 260 SDSS quasars at $1.55 \lesssim z \lesssim 3.50$. This catalog includes basic spectral properties of rest-frame optical emission lines, chiefly the Mg II, Hβ, [O III], Fe II, and Hα lines, depending on the availability of the line in the spectrum. These measurements provide an enhancement to the existing GNIRS-DQS database enabling one to more accurately analyze and investigate rest-frame UV-optical spectral properties for high-redshift, high-luminosity quasars in a manner consistent with studies of low-redshift quasars.

We also present prescriptions for correcting UV-based redshifts based on a subset of the GNIRS-DQS sample of 121 sources that are non-BAL, non-RL, have accurate C IV measurements, and have z_{sys} values obtained from prominent [O III] measurements. We provide measurements of velocity offsets using three different UV-based methods compared to z_{sys} values. This 121-source sample is over twice the size of the calibration sample used in D20 and is both a higher quality and more uniform data set than M17 and D20.

We attempt to correct for these velocity offsets using a linear regression based on UV continuum luminosity and C IV emission-line properties. Using this approach, we can decrease the standard deviation of the distribution of velocity offsets in our calibration sample by ∼2% with respect to the best available UV-based redshift method and by ∼18% with respect to C IV-based redshifts. The SDSS Pipeline provides the least precise

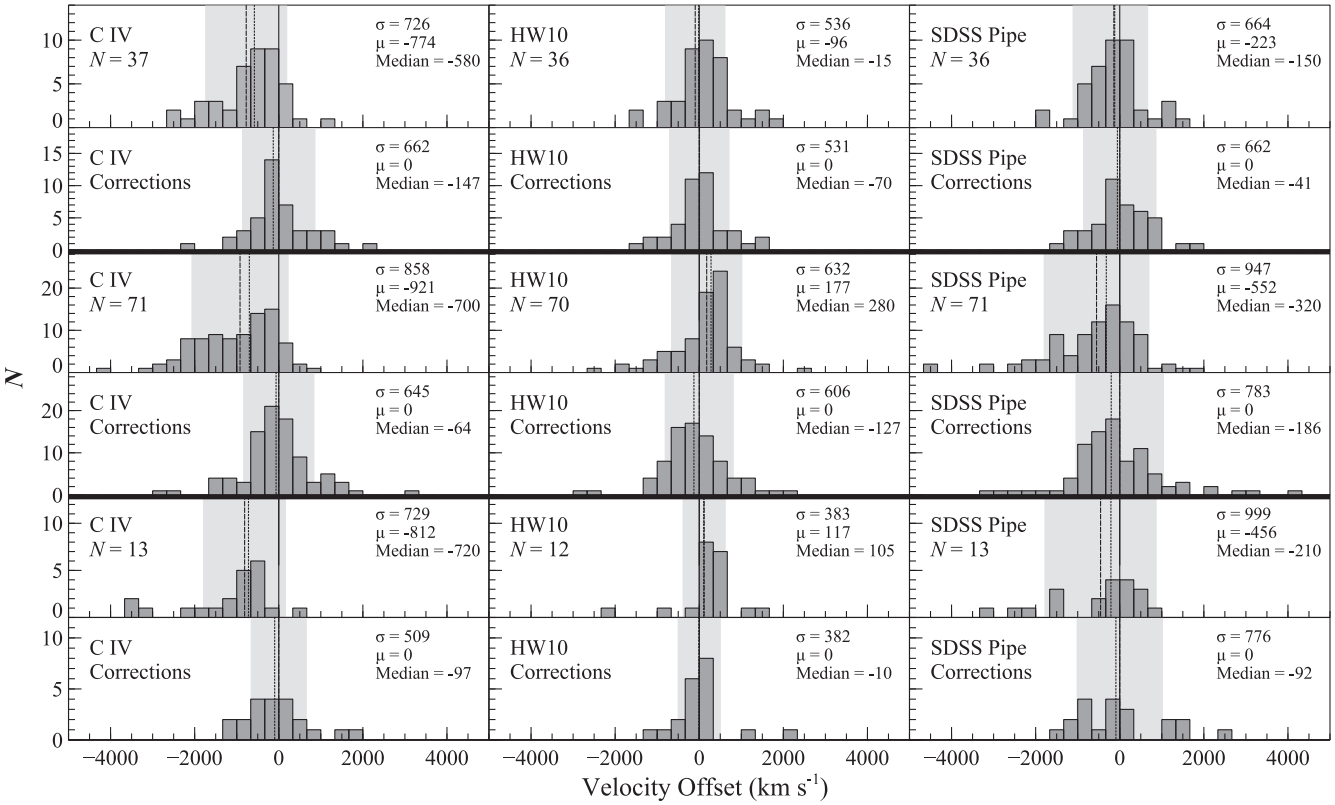

Figure 7. Same as Figure 4, but split into three redshift bins. Top six panels, middle six panels, and bottom six panels correspond to redshift Bin 1, Bin 2, and Bin 3, respectively, as described in the text.

UV-based redshifts; in particular, the standard deviation of the corrected redshifts is still ∼20% larger than those achieved for the other two methods. We find that the best way to obtain an accurate and precise $z_{\rm sys}$ value is using the C IV parameter space alone via four basic observables associated with the C IV emission line and applying the following methodology:

1. Measure the observed peak wavelength, EW, and FWHM of C IV, and the monochromatic luminosity at 1350 Å (L_{1350}).
2. Calculate an initial redshift measurement, $z_{\rm meas}$, with the observed peak wavelength of C IV.
3. Use Equation (2) and the coefficients in Table 6 to calculate $\Delta v_{\rm corr}$.
4. Use Equation (3) with the observed $z_{\rm meas}$ and calculated $\Delta v_{\rm corr}$ to obtain a revised, more accurate, and more precise redshift measurement.

Additionally, we explore whether our prescriptions depend on (1) velocity width measurement, of which we determine there is no overt discrepancy based on methodology, (2) source redshift, where we determine that additional data are needed, particularly at the highest redshifts under investigation, in order to obtain more robust results, and (3) source luminosity, where no clear trends are apparent, consistent with the flux-limited nature of our sample.

A primary interest going forward would be bolstering the sample with supplementary observations of quasars, primarily at $z \sim 3$, in order to obtain statistically meaningful results on a potential redshift dependence, and further improve UV-based redshift determinations. It will also be interesting to test our prescriptions at the highest accessible redshifts, where considerably larger C IV blueshifts have been observed in sources at $z \gtrsim 6$, perhaps due to higher accretion rates (e.g., Meyer et al. 2019; Schindler et al. 2020; Ha et al. 2023). Another avenue of further investigation includes increasing the sample size of quasars with significantly higher spectral resolution, e.g., using Gemini's Spectrograph and Camera for Observations of Rapid Phenomena in the Infrared and Optical (Robberto et al. 2020), in order to further improve the UV-based redshift corrections by obtaining more accurate line peaks of spectral features. Machine learning can also play an important role as larger data sets will be produced that require redshift correction en masse. By utilizing the entire quasar UV spectrum, as opposed to a few key parameters, it will be possible to test if machine-learning algorithms can produce more reliable estimates of $z_{\rm sys}$ much more efficiently than our prescriptions allow.

As future projects begin to produce data, we can expect that $\approx 10^6$ high-redshift ($z \gtrsim 0.8$) quasars will have redshifts determined through large spectroscopic surveys conducted in the rest-frame UV-optical regime from instruments such as the Dark Energy Spectroscopic Instrument (DESI; Levi et al. 2013; DESI Collaboration et al. 2016), the 4 m Multi-Object Spectroscopic Telescope (de Jong et al. 2012), and the Subaru Prime Focus Spectrograph (Tamura et al. 2016). For those quasars at $1.5 \lesssim z \lesssim 5.0$, coverage of the C IV emission line will enable crucial redshift corrections, as has been demonstrated in this work. Instruments such as the James Webb Space Telescope (Gardner et al. 2006) can provide simultaneous coverage of C IV, Mg II, and [O III], while other facilities can provide other systemic redshift indicators such as [C II], CO, and Lyα halos (see, e.g., Decarli et al. 2018; Farina et al. 2019) for $6 \lesssim z \lesssim 9$, allowing for similar investigations of redshift dependencies and corrections for the most distant known quasars.

Acknowledgments

This work is supported by National Science Foundation grants AST-1815281 (B. M. M., C. D., O. S.) and AST-1815645 (M. S. B., A. D. M., J. N. M.). W.N.B. acknowledges support from NSF grant AST-2106990. We thank an anonymous referee for thoughtful and valuable comments that helped improve this paper. This work was enabled by observations made from the Gemini North telescope, located within the Maunakea Science Reserve and adjacent to the summit of Maunakea. We are grateful for the privilege of observing the universe from a place that is unique in both its astronomical quality and its cultural significance. This research has made use of the NASA/IPAC Extragalactic Database (NED), which is operated by the Jet Propulsion Laboratory, California Institute of Technology, under contract with the National Aeronautics and Space Administration. We thank Paul Hewett for helpful contributions of redshift data.

Appendix
Comparing Different Velocity Widths of the C IV Line

In our regression analysis, we have elected to use the FWHM of the C IV line. However, there has been some debate in the literature concerning the overall reliability of using FWHM as

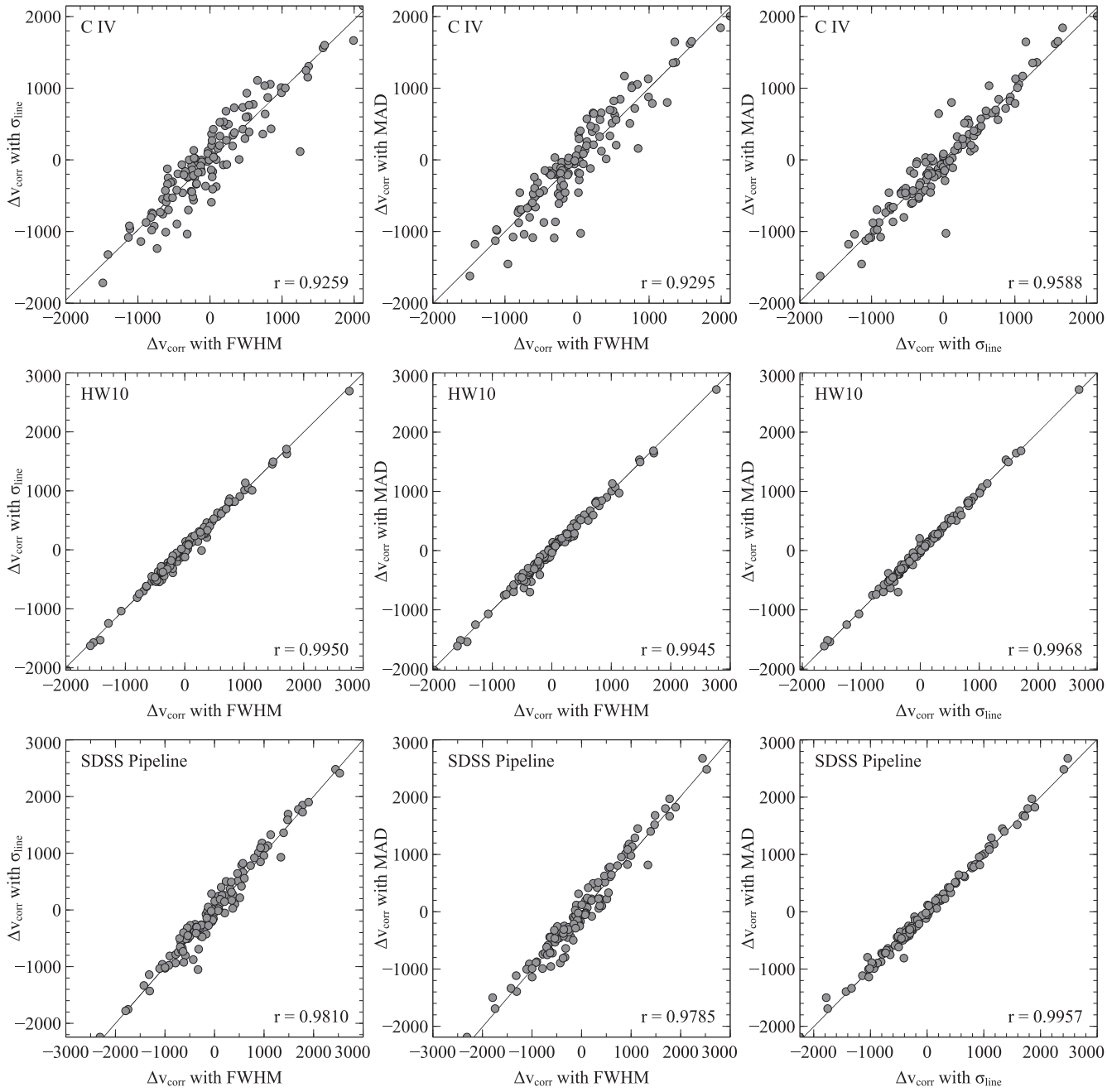

Figure A1. Comparison of the velocity offsets produced using C IV FWHM, $\sigma_{\rm line}$, and MAD for each UV-based redshift method. Each panel displays the correlation between the corrected velocity offset values produced by our regression analysis when using either FWHM, $\sigma_{\rm line}$, or MAD, along with a corresponding Pearson linear correlation coefficient r, where $r \rightarrow 1$ corresponds to a strong correlation. No significant difference exists in this regression analysis between the three different parameters.

the quantification of the velocity width of an emission line (e.g., Park et al. 2017; Dalla Bontà et al. 2020). While M17 and D20 used FWHM for their analyses, other methods for measuring velocity widths of emission-line profiles include line dispersion ($\sigma_{\rm line}$) and mean absolute deviation (MAD; e.g., Denney et al. 2016; Dalla Bontà et al. 2020). We therefore repeated our analysis by replacing FWHM with each of these two velocity width methods, measured from the Gaussian fits presented in Table 4, and compared the results obtained from all three velocity widths. We find that replacing FWHM with $\sigma_{\rm line}$ or MAD gave no notable improvement in the dispersion on the relevant corrections, as shown in Figure A1. We thus have elected to adopt the FWHM parameterization throughout this work.

ORCID iDs

Brandon M. Matthews https://orcid.org/0000-0001-8406-4084
Cooper Dix https://orcid.org/0000-0003-0192-1840
Ohad Shemmer https://orcid.org/0000-0003-4327-1460
Michael S. Brotherton https://orcid.org/0000-0002-1207-0909
I. Andruchow https://orcid.org/0000-0003-1562-5188
W. N. Brandt https://orcid.org/0000-0002-0167-2453
S. C. Gallagher https://orcid.org/0000-0001-6217-8101
Richard Green https://orcid.org/0000-0003-1245-5232
Paulina Lira https://orcid.org/0000-0003-1523-9164
Jacob N. McLane https://orcid.org/0000-0003-1081-2929
Richard M. Plotkin https://orcid.org/0000-0002-7092-0326
Gordon T. Richards https://orcid.org/0000-0002-1061-1804
Jessie C. Runnoe https://orcid.org/0000-0001-8557-2822
Donald P. Schneider https://orcid.org/0000-0001-7240-7449
Michael A. Strauss https://orcid.org/0000-0002-0106-7755

References

Alcock, C., & Paczynski, B. 1979, Natur, 281, 358
Begelman, M., de Kool, M., & Sikora, M. 1991, ApJ, 382, 416
Bolton, A. S., Schlegel, D. J., Aubourg, É., et al. 2012, AJ, 144, 144
Boroson, T. 2005, AJ, 130, 381
Boroson, T. A., & Green, R. F. 1992, ApJS, 80, 109
Carniani, S., Maiolino, R., Marconi, A., et al. 2018, in AGN13: Beauty and the Beast. The XIII Italian Meeting on Active Galactic Nuclei, v1, Zenodo, doi:10.5281/zenodo.1481694
Coatman, L., Hewett, P. C., Banerji, M., et al. 2017, MNRAS, 465, 2120
Dalla Bontà, E., Peterson, B. M., Bentz, M. C., et al. 2020, ApJ, 903, 112
Dawson, K. S., Schlegel, D. J., Ahn, C. P., et al. 2013, AJ, 145, 10
DESI Collaboration, Aghamousa, A., Aguilar, J., et al. 2016, arXiv:1611.00036
de Jong, R. S., Bellido-Tirado, O., Chiappini, C., et al. 2012, Proc. SPIE, 8446, 84460T
Decarli, R., Walter, F., Venemans, B. P., et al. 2018, ApJ, 854, 97
Denney, K. D., Horne, K., Shen, Y., et al. 2016, ApJS, 224, 14
Dix, C., Matthews, B. M., Shemmer, O., et al. 2023, ApJ, 950, 96
Dix, C., Shemmer, O., Brotherton, M. S., et al. 2020, ApJ, 893, 14
Farina, E. P., Arrigoni-Battaia, F., Costa, T., et al. 2019, ApJ, 887, 196
Font-Ribera, A., Arnau, E., Miralda-Escudé, J., et al. 2013, JCAP, 2013, 018
Gardner, J. P., Mather, J. C., Clampin, M., et al. 2006, SSRv, 123, 485
Gaskell, C. M. 1982, ApJ, 263, 79
Gibson, R. R., Jiang, L., Brandt, W. N., et al. 2009, ApJ, 692, 758
Ha, T., Dix, C., Matthews, B. M., Shemmer, O., et al. 2023, ApJ, 950, 97
Hewett, P. C., & Wild, V. 2010, MNRAS, 405, 2302
Hogg, D. W. 1999, arXiv:astro-ph/9905116
Hopkins, P. F., & Elvis, M. 2010, MNRAS, 401, 7
Kellermann, K. I., Sramek, R., Schmidt, M., Shaffer, D. B., & Green, R. 1989, AJ, 98, 1195
Levi, M., Bebek, C., Beers, T., et al. 2013, arXiv:1308.0847
Lyke, B. W., Higley, A. N., McLane, J. N., et al. 2020, ApJS, 250, 8
Maiolino, R., Gallerani, S., Neri, R., et al. 2012, MNRAS Lett., 425, L66
Mason, M., Brotherton, M. S., & Myers, A. 2017, MNRAS, 469, 4675
Matthews, B. M., Shemmer, O., Dix, C., et al. 2021, ApJS, 252, 15
McGreer, I. D., Eftekharzadeh, S., Myers, A. D., & Fan, X. 2016, AJ, 151, 61
Meyer, R. A., Bosman, S. E. I., & Ellis, R. S. 2019, MNRAS, 487, 3305
Miller, B. P., Brandt, W. N., Schneider, D. P., et al. 2011, ApJ, 726, 20
Murray, N., Chiang, J., Grossman, S. A., & Voit, G. M. 1995, ApJ, 451, 498
Nguyen, N. H., Lira, P., Trakhtenbrot, B., et al. 2020, ApJ, 895, 74
Pâris, I., Petitjean, P., Aubourg, É., et al. 2018, A&A, 613, A51
Pâris, I., Petitjean, P., Ross, N. P., et al. 2017, A&A, 597, A79
Park, D., Barth, A. J., Woo, J.-H., et al. 2017, ApJ, 839, 93
Rankine, A. L., Hewett, P. C., Banerji, M., & Richards, G. T. 2020, MNRAS, 492, 4553
Richards, G. T., Kruczek, N. E., Gallagher, S. C., et al. 2011, AJ, 141, 167
Rivera, A. B., Richards, G. T., Hewett, P. C., & Rankine, A. L. 2020, ApJ, 899, 96
Robberto, M., Roming, P. W. A., van der Horst, A. J., et al. 2020, Proc. SPIE, 11447, 1144774
Schindler, J.-T., Farina, E. P., Bañados, E., et al. 2020, ApJ, 905, 51
Schneider, D. P., Richards, G. T., Hall, P. B., et al. 2010, AJ, 139, 2360
Shen, Y., Brandt, W. N., Richards, G. T., et al. 2016, ApJ, 831, 7
Shen, Y., Greene, J. E., Strauss, M. A., Richards, G. T., & Schneider, D. P. 2008, ApJ, 680, 169
Shen, Y., Richards, G. T., Strauss, M. A., et al. 2011, ApJS, 194, 45
Shen, Y., Strauss, M. A., Oguri, M., et al. 2007, AJ, 133, 2222
Sheskin, D. J. 2007, Handbook of Parametric and Nonparametric Statistical Procedures (4th ed.; New York: Chapman & Hall/CRC)
Spergel, D. N., Bean, R., Doré, O., et al. 2007, ApJS, 170, 377
Sulentic, J. W., Bachev, R., Marziani, P., Negrete, C. A., & Dultzin, D. 2007, ApJ, 666, 757
Tamura, N., Takato, N., Shimono, A., et al. 2016, Proc. SPIE, 9908, 99081M
Tytler, D., & Fan, X.-M. 1992, ApJS, 79, 1
Vanden Berk, D. E., Richards, G. T., Bauer, A., et al. 2001, AJ, 122, 549
Vietri, G., Piconcelli, E., Bischetti, M., et al. 2018, A&A, 617, A81
York, D. G., Adelman, J., Anderson, J. E., et al. 2000, AJ, 120, 1579
Zhao, G.-B., Wang, Y., Saito, S., et al. 2019, MNRAS, 482, 3497